



# A transition metal oxysulfide cathode for the proton exchange membrane water electrolyzer

Hyunki Kim<sup>a</sup>, Junhyeong Kim<sup>a</sup>, Soo-Kil Kim<sup>b,\*</sup>, Sang Hyun Ahn<sup>a,\*</sup>

<sup>a</sup> School of Chemical Engineering and Material Science, Chung-Ang University, 84 Heukseok-ro, Dongjak-gu, Seoul, 06974, Republic of Korea

<sup>b</sup> School of Integrative Engineering, Chung-Ang University, 84 Heukseok-ro, Dongjak-gu, Seoul, 06974, Republic of Korea

## ARTICLE INFO

### Keywords:

Transition metal oxysulfide  
Proton exchange membrane water electrolyzer  
Hydrogen evolution reaction  
Electrodeposition  
Anion exchange reaction

## ABSTRACT

In this study, the performance of transition metal oxysulfides as cathodes has been explored for a proton exchange membrane water electrolyzer (PEMWE). Simple electrodeposition and anion exchange methods provide facile control of the morphology and composition of  $\text{Ni}_y\text{Co}_{1-y}\text{O}_x\text{S}_z$  catalysts deposited as gas diffusion electrodes on carbon paper substrates. After sulfidation, the overpotential for the hydrogen evolution reaction (HER) was significantly reduced and the intrinsic activity of the HER showed volcano behaviors as a function of the composition and binding energy of S in the electrodes. The PEMWE employing such a cathode demonstrates a reasonable current density of  $0.72 \text{ A/cm}^2$  at a cell voltage of 2.0 V. The results presented herein demonstrate that the non-noble catalyst can be adopted as a cathode in PEMWE operation.

## 1. Introduction

Eco-friendly hydrogen has attracted much attention as an alternative energy source to fossil fuels in the near future [1,2]. Beyond conventional methods [3,4], hydrogen production through a water electrolyzer is promising because hydrogen can be obtained without carbon dioxide emission during electrochemical reactions under moderate operating conditions [5–7]. In particular, the PEMWE has the advantage that higher purity hydrogen can be produced at a faster rate compared to the other electrolyzers [6]. However, its practical application in industries for mass hydrogen production is still limited owing to its high costs and lower efficiencies compared to the conventional method. To solve these problems, it is essential to develop a low-cost catalyst having high activity and stability. For the cathode of the PEMWE, Pt is known to be the catalyst that can best facilitate the HER [8]; however, its high price presents a technical bottleneck [9,10]. Nonetheless, many studies have been performed on the development of Pt-based alloys [11] or core-shells [12,13]. Alternatively, transition metal compounds including carbides [14,15], nitrides [16,17], phosphides [18,19], and sulfides [20,21] have been actively investigated for acidic HER.

Among them, the catalytic activities of various transition metal sulfides such as  $\text{NiS}_x$  [22,23],  $\text{CoS}_2$  [24,25],  $\text{FeS}_2$  [26,27], and  $\text{MoS}_x$  [28,29] have been examined. The origin of their higher HER activities than pure transition metals has been attributed to the suitable energies for hydrogen adsorption on the catalyst surfaces [30–32]. To fabricate

the transition metal sulfide, a sulfidation process on the metal surface is essential and is typically performed in a furnace with  $\text{H}_2\text{S}$  gas flow at a high temperature and atmospheric pressure [33]. However, it has disadvantages such as costly equipment, process complexity, and long processing times. Nevertheless, the sulfur ion exchange reaction (IER) in aqueous solutions based on a difference in solubility product constants ( $K_{sp}$ ) presents a very easy and simple process because it proceeds at a relatively low temperature and ambient pressure [34–40]. In common, the materials having lower  $K_{sp}$  values indicate more thermodynamically stable compared to that having higher  $K_{sp}$  values [36]. As many transition metal oxides or hydroxides have  $K_{sp}$  values higher than those of the metal sulfides, they can be spontaneously converted to the sulfide form in an aqueous solution containing  $\text{S}^{2-}$ . For example, the  $K_{sp}$  values of oxide, hydroxide, and sulfide for Ni and Co are reported as  $\text{NiO}$  ( $1.5 \times 10^{-17}$ ),  $\text{Co}_3\text{O}_4$  ( $3.1 \times 10^{-18}$ ),  $\text{Ni(OH)}_2$  ( $5.9 \times 10^{-15}$ ),  $\text{NiS}$  ( $1.3 \times 10^{-25}$ ), and  $\text{CoS}$  ( $3 \times 10^{-26}$ ) [36]. Based on the IER method,  $\text{CoS}$  [37],  $\text{NiCo}$ -layered double hydroxide nanoflakes ( $\text{NiCo-LDH/Ni}$  foam) [34],  $\text{Ni}_2\text{S}_3$  [38], graphdiyne-supported  $\text{NiCo}_2\text{S}_4$  nanowires ( $\text{NiCo}_2\text{S}_4 \text{ NW/GDF}$ ) [39],  $\text{NiCo}$  sulfide (NC-S) [40], etc. were manufactured, and their catalytic activities for the HER were tested under acidic and alkaline conditions.

Recently, the HER catalytic performance of Co oxysulfide under alkaline condition has been reported [41]. After the synthesis of  $\text{CoO}_x$  nanoparticle (NP), the partial anionic substitution was performed by S IER to fabricate  $\text{CoO}_x\text{S}_y$  NPs. The density functional theory (DFT) result showed the change in hydrogen adsorption energy on the surface of

\* Corresponding authors.

E-mail addresses: [sookilkim@cau.ac.kr](mailto:sookilkim@cau.ac.kr) (S.-K. Kim), [shahn@cau.ac.kr](mailto:shahn@cau.ac.kr) (S.H. Ahn).

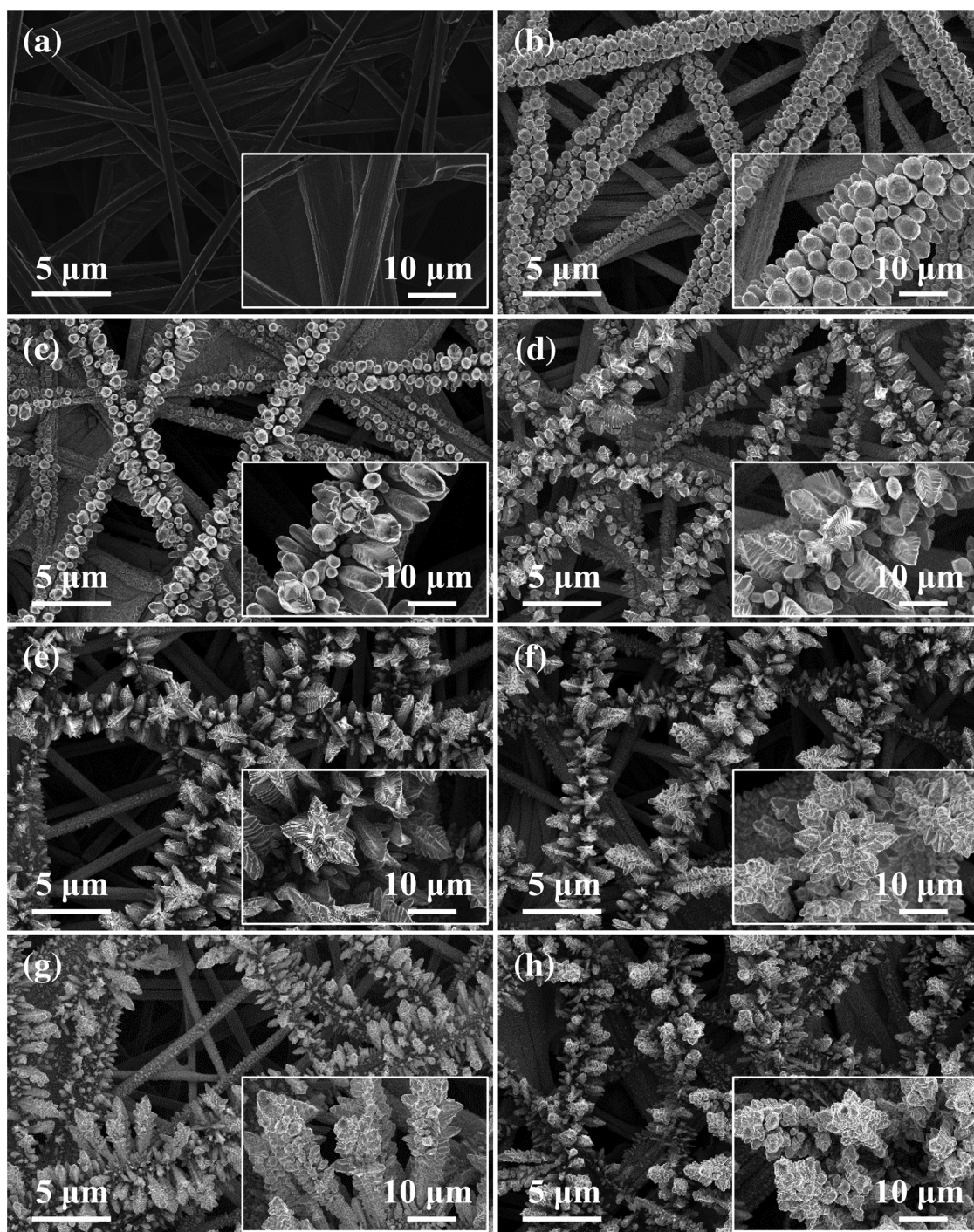


**Fig. 1.** FESEM images of (a) annealed CP, (b)  $\text{NiO}_x/\text{CP}$ , (c)  $\text{Ni}_{0.80}\text{Co}_{0.20}\text{O}_x/\text{CP}$ , (d)  $\text{Ni}_{0.60}\text{Co}_{0.40}\text{O}_x/\text{CP}$ , (e)  $\text{Ni}_{0.51}\text{Co}_{0.49}\text{O}_x/\text{CP}$ , (f)  $\text{Ni}_{0.39}\text{Co}_{0.61}\text{O}_x/\text{CP}$ , (g)  $\text{Ni}_{0.20}\text{Co}_{0.80}\text{O}_x/\text{CP}$ , and (h)  $\text{CoO}_x/\text{CP}$ . Insets: FESEM images displayed at a higher magnification.

$\text{CoO}$  (100) as O is gradually substituted by S. At an S ratio of 0.18, the hydrogen adsorption energy became optimal for the HER, with the experimental results showing the highest specific activity of  $-0.043 \text{ mA}/\text{cm}^2$  at 375 mV overpotential, which is 2.87 times higher than that of  $\text{CoO}_x$  under the same conditions. Another example is the fullerene-like nickel oxysulfide hollow nanospheres (FNHNs) [42]. Under alkaline conditions, overpotential at  $-10 \text{ mA}/\text{cm}^2$  was 60 mV higher than that of the Ni foam. When the FNHNs was formed on Ni foam to increase the surface area, it was reduced by 90 mV compared to Ni foam. However, most results with sulfides and oxysulfides mentioned above are limited in the half-cell measurement. The PEMWE operation employing transition metal alloy and sulfide cathodes is

rarely found:  $\text{Fe}_x\text{S}_y$  [43],  $\text{Cu}_{93.7}\text{Mo}_{0.63}$  [44],  $\text{MoS}_2$ -carbon composites [45], amorphous  $\text{MoS}_x$  [46], and  $\text{MoS}_2$  nanocapsule [47]. The PEMWE with the non-noble cathodes exhibited the current density of  $0.35\text{--}0.73 \text{ A}/\text{cm}^2$  at 2.0 V in the operating temperature range of  $80\text{--}90^\circ\text{C}$  [43–45] which were still lower than that with noble Pt/C cathodes ( $1.46\text{--}2.71 \text{ A}/\text{cm}^2$ ) [48–52]. Furthermore, to the best of our knowledge, the performance of transition metal oxysulfide cathodes for the PEMWE operation has not been reported.

In this study, a transition metal oxysulfide ( $\text{Ni}_y\text{Co}_{1-y}\text{O}_x\text{S}_z$ ) catalyst was fabricated directly on a carbon paper (CP) substrate and the performance of a single cell was evaluated by using it as the cathode of the PEMWE. The  $\text{Ni}_y\text{Co}_{1-y}\text{O}_x$  catalyst was synthesized on CP using a two-



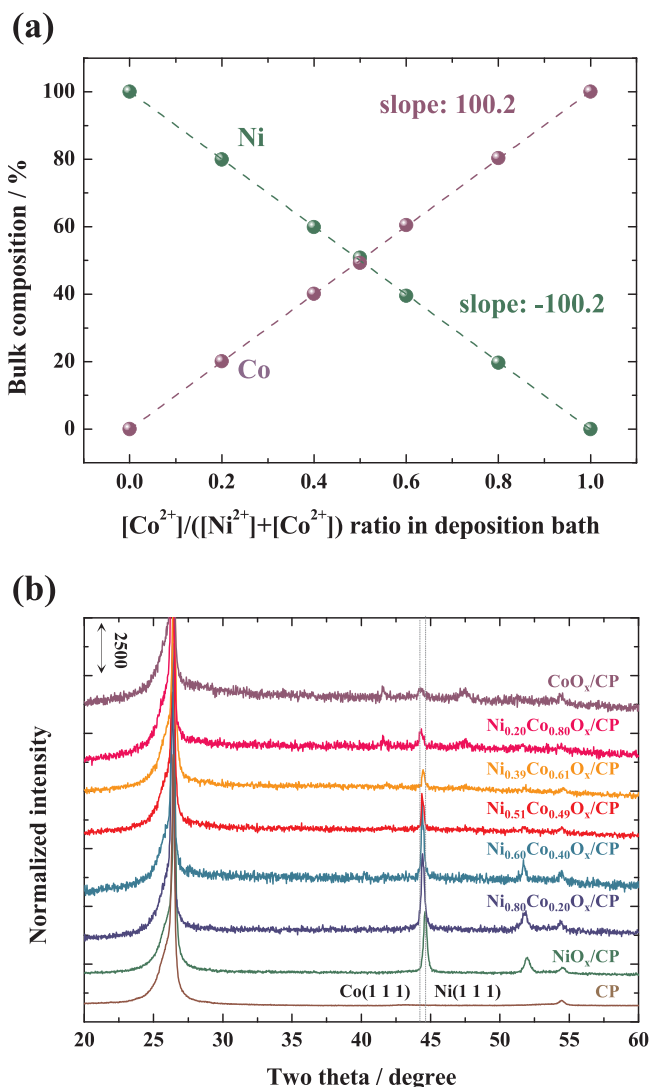


Fig. 2. (a) Bulk compositions of electrodeposits as a function of the  $\text{Co}^{2+}$  precursor ratio in the electrodeposition bath. (b) XRD patterns of electrodeposited  $\text{NiO}_x/\text{CP}$ ,  $\text{Ni}_y\text{Co}_{1-y}\text{O}_x/\text{CP}$ , and  $\text{CoO}_x/\text{CP}$ .

step electrodeposition method. The morphology of  $\text{Ni}_y\text{Co}_{1-y}\text{O}_x/\text{CP}$  changed from spherical to having a fern-like shape depending on the concentration of the  $\text{Co}^{2+}$  precursor in the deposition bath at a constant current and time. Subsequently, the partial replacement of O with S by the S IER facilitates the fabrication of the  $\text{Ni}_y\text{Co}_{1-y}\text{O}_x\text{S}_z/\text{CP}$  catalyst. After the sulfidation process, the HER was significantly enhanced. From the measured electrochemical surface area, the intrinsic HER activity was obtained, and was shown to be strongly affected by S composition and the proportion of highly oxidized S atoms. Furthermore, the

Table 1

Summary of catalyst composition, electrochemical properties, and HER performance.

Catalysts		Overpotential at $-10 \text{ mA}/\text{cm}_{\text{geo}}^2$ (mV)	Tafel slope (mV/dec)	Exchange current density ( $\text{mA}/\text{cm}_{\text{geo}}^2$ )	$C_{\text{dl}}$ (mF/ $\text{cm}_{\text{geo}}^2$ )	Scaled exchange current ( $\text{mA}/\text{mF}$ )	S higher binding energy ratio (%)
Before S IER	After S IER						
$\text{NiO}_x/\text{CP}$	$\text{NiO}_{x0.14}/\text{CP}$	188	83.7	0.056	5.58	0.0100	38.0
$\text{Ni}_{0.80}\text{Co}_{0.20}\text{O}_x/\text{CP}$	$\text{Ni}_{0.78}\text{Co}_{0.22}\text{O}_{x0.25}\text{S}_{0.25}/\text{CP}$	183	80.5	0.054	4.44	0.0122	36.2
$\text{Ni}_{0.60}\text{Co}_{0.40}\text{O}_x/\text{CP}$	$\text{Ni}_{0.64}\text{Co}_{0.36}\text{O}_{x0.28}\text{S}_{0.28}/\text{CP}$	172	78.0	0.064	8.74	0.0074	33.3
$\text{Ni}_{0.51}\text{Co}_{0.49}\text{O}_x/\text{CP}$	$\text{Ni}_{0.47}\text{Co}_{0.53}\text{O}_{x0.38}\text{S}_{0.38}/\text{CP}$	179	67.8	0.023	6.52	0.0035	29.9
$\text{Ni}_{0.39}\text{Co}_{0.61}\text{O}_x/\text{CP}$	$\text{Ni}_{0.48}\text{Co}_{0.52}\text{O}_{x0.47}\text{S}_{0.47}/\text{CP}$	181	68.8	0.024	7.54	0.0032	26.8
$\text{Ni}_{0.20}\text{Co}_{0.80}\text{O}_x/\text{CP}$	$\text{Ni}_{0.29}\text{Co}_{0.71}\text{O}_{x0.56}\text{S}_{0.56}/\text{CP}$	214	85.3	0.031	8.82	0.0035	28.0
$\text{CoO}_x/\text{CP}$	$\text{CoO}_{x0.31}/\text{CP}$	N/A	N/A	N/A	8.53	N/A	20.1

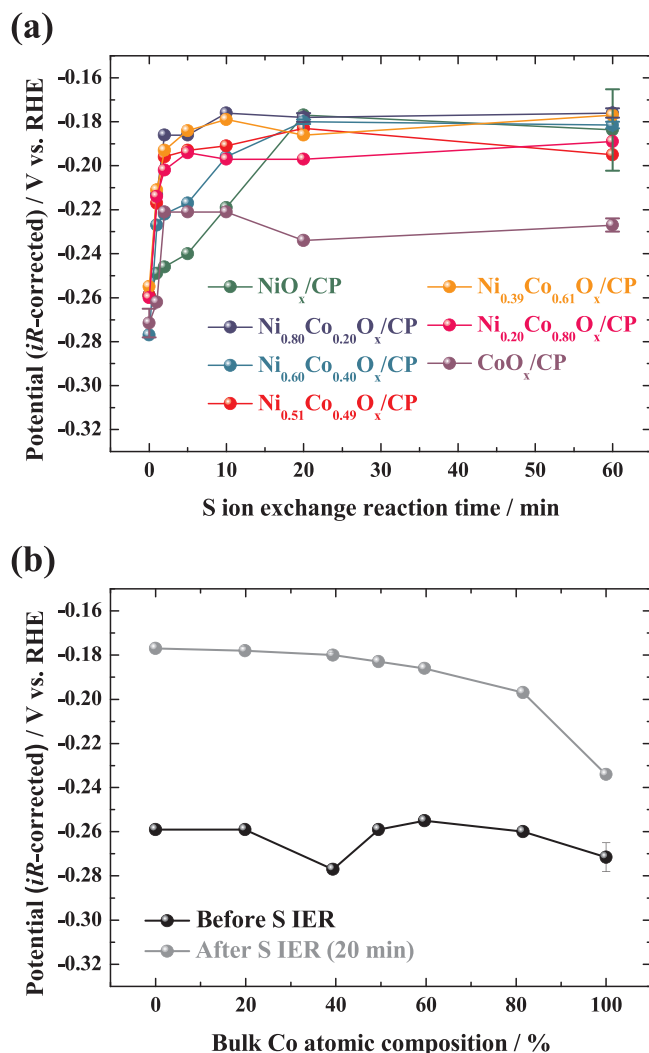


Fig. 3. (a) The HER overpotential at  $-10 \text{ mA}/\text{cm}_{\text{geo}}^2$  current density as a function of S IER time, (b) the overpotential at  $-10 \text{ mA}/\text{cm}_{\text{geo}}^2$  before and after S IER (reaction time 20 min).

PEMWE employing the transition metal oxysulfide cathode demonstrated a reasonable performance.

## 2. Experimental

### 2.1. Preparation of fern-like $\text{Ni}_y\text{Co}_{1-y}\text{O}_x\text{S}_z/\text{CP}$

The solution for electrodeposition was composed of  $\text{NiCl}_2 \cdot 6\text{H}_2\text{O}$  (98.0%, DAEJUNG),  $\text{CoCl}_2 \cdot 6\text{H}_2\text{O}$  (98.0%, DAEJUNG), and  $\text{H}_3\text{BO}_3$  (99.5%, DAEJUNG). The concentrations of the two metal precursors

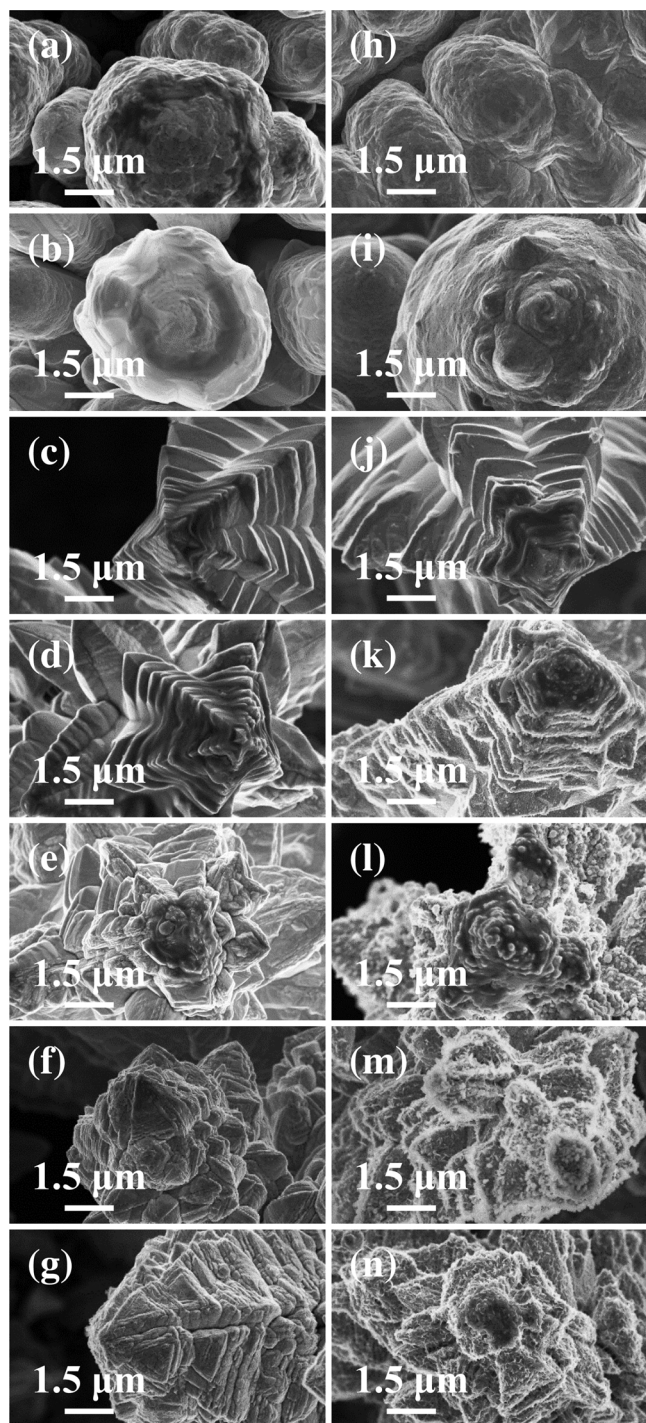


**Fig. 4.** FESEM images of  $\text{Ni}_y\text{Co}_{1-y}\text{O}_x/\text{CP}$  (a–g) before IER and (h–n) after IER for 20 min. (a) corresponds to  $\text{NiO}_x/\text{CP}$ , (b)  $\text{Ni}_{0.80}\text{Co}_{0.20}\text{O}_x/\text{CP}$ , (c)  $\text{Ni}_{0.60}\text{Co}_{0.40}\text{O}_x/\text{CP}$ , (d)  $\text{Ni}_{0.51}\text{Co}_{0.49}\text{O}_x/\text{CP}$ , (e)  $\text{Ni}_{0.39}\text{Co}_{0.61}\text{O}_x/\text{CP}$ , (f)  $\text{Ni}_{0.20}\text{Co}_{0.80}\text{O}_x/\text{CP}$ , (g)  $\text{CoO}_x/\text{CP}$ , (h)  $\text{NiO}_x\text{S}_{0.14}/\text{CP}$ , (i)  $\text{Ni}_{0.78}\text{Co}_{0.22}\text{O}_x\text{S}_{0.25}/\text{CP}$ , (j)  $\text{Ni}_{0.64}\text{Co}_{0.36}\text{O}_x\text{S}_{0.28}/\text{CP}$ , (k)  $\text{Ni}_{0.47}\text{Co}_{0.53}\text{O}_x\text{S}_{0.38}/\text{CP}$ , (l)  $\text{Ni}_{0.48}\text{Co}_{0.52}\text{O}_x\text{S}_{0.47}/\text{CP}$ , (m)  $\text{Ni}_{0.29}\text{Co}_{0.71}\text{O}_x\text{S}_{0.56}/\text{CP}$ , and (n)  $\text{CoO}_x\text{S}_{0.31}/\text{CP}$ .

were varied while maintaining the total concentration (0.1 M), whereas the concentration of  $\text{H}_3\text{BO}_3$  was fixed at 0.5 M. All the solutions used in the experiment were treated with  $\text{N}_2$  gas bubbles for 30 min. The electrodeposition was carried out in a three-electrode cell system controlled using a potentiostat (Autolab PGSTAT302N, Metrohm). The CP (TGPH-090, Toray) substrate was used as the working electrode. As pretreatment, an annealing process was performed on the CP in a tube furnace at  $800^\circ\text{C}$  for 10 min to render it more hydrophilic [53]. The

pretreated CP was sealed with a lab-made Teflon cell and had an exposed area of  $1.13\text{ cm}^2$ . A Pt wire and saturated calomel electrode (SCE; KCl saturated) were used as the counter and reference electrodes, respectively. The fern-like  $\text{Ni}_y\text{Co}_{1-y}\text{O}_x/\text{CP}$  was prepared by a two-step galvanostatic method using a current density  $-3\text{ mA}/\text{cm}^2$  for 300 s, followed by  $-55\text{ mA}/\text{cm}^2$  for another 300 s under room temperature and atmospheric pressure [54]. After electrodeposition, the samples were rinsed with deionized water and blown with  $\text{N}_2$  gas.

The electrodeposited  $\text{Ni}_y\text{Co}_{1-y}\text{O}_x/\text{CP}$  was immersed in a 1 mM  $\text{Na}_2\text{S}\cdot 5\text{H}_2\text{O}$  solution (98.0%, DAEJUNG) under room temperature and atmospheric pressure [36]. The S IER time was maintained between 1 min and 60 min. Subsequently, the prepared  $\text{Ni}_y\text{Co}_{1-y}\text{O}_x\text{S}_z/\text{CP}$  was rinsed with deionized water and blown with  $\text{N}_2$  gas.

## 2.2. Characterization

Field emission scanning electron microscopy (FESEM; SIGMA, Carl Zeiss) was used to image the surface morphology of the prepared samples. To analyze the bulk and surface composition, energy dispersive spectroscopy (EDS, Thermo NORAN System 7) and X-ray photoelectron spectroscopy (XPS, K-alpha+, ThermoFisher Scientific) were adopted, respectively. The crystal structure of the samples was investigated using X-ray diffraction (XRD; New D8-Advance, BRUKER). To determine the electrochemical active surface area, the double layer capacitance ( $C_{dl}$ ) was measured by varying the scan rate of cyclic voltammetry (CV) in 1.0 M KOH. The measurement was repeated to stabilize the current density.

## 2.3. HER activity test

The electrochemical test was performed in a three-electrode cell system using a potentiostat (Autolab PGSTAT302N, Metrohm). The fabricated catalysts were used as working electrodes. The graphite rod and saturated calomel electrode (SCE, KCl saturated) were used as a counter and a reference electrode, respectively. In the  $\text{N}_2$ -purged 0.5 M  $\text{H}_2\text{SO}_4$  electrolyte (95.0%, JUNSEI), the HER activity was measured using chronopotentiometry at  $-10\text{ mA}/\text{cm}_{\text{geo}}^2$  for 100 s and CV in the potential range  $-0.4$  to  $-0.8\text{ V}_{\text{SCE}}$  at a scan rate of  $50\text{ mV}/\text{s}$ . All measured potentials were converted to reversible hydrogen electrode (RHE).

## 2.4. PEMWE operation

The membrane electrode assembly (MEA) for the PEMWE single cell was fabricated by sandwiching a Nafion membrane (212, Dupont. Co.) between the cathode and anode. The electrodeposited  $\text{Ni}_y\text{Co}_{1-y}\text{O}_x\text{S}_z/\text{CP}$  was used as the cathode whereas the electrodeposited  $\text{IrO}_2/\text{CP}$  (loading mass of  $\text{IrO}_2$ :  $0.1\text{ mg}/\text{cm}^2$ ) was employed as the anode [48]. The active area of the cell was  $1\text{ cm} \times 1\text{ cm}$ . The fabricated cell temperature was maintained at  $90^\circ\text{C}$  and the preheated 18 MΩ deionized water at  $90^\circ\text{C}$  was injected with a rate of 15 ccm. The applied potential was increased from 1.5 V to 2.3 V by an interval of 0.05 V and each potential was maintained for 1 min.

## 3. Results and discussion

### 3.1. Preparation and characterization of fern-like $\text{Ni}_y\text{Co}_{1-y}\text{O}_x/\text{CP}$

Fig. 1a shows the pretreated CP substrate annealed at  $800^\circ\text{C}$  for 10 min. Electrodeposition was carried out using a two-step galvanostatic method involving a low current density ( $-3\text{ mA}/\text{cm}^2$ ) for 300 s to increase adhesion followed by a high current density ( $-55\text{ mA}/\text{cm}^2$ ) for 300 s to obtain a three-dimensional structure with a large surface area. Fig. 1b–h shows the  $\text{NiO}_x$ ,  $\text{Ni}_y\text{Co}_{1-y}\text{O}_x$ , and  $\text{CoO}_x$  deposits on the annealed CP with varying Ni and Co precursor compositions in the deposition bath. Without the Co precursor (Fig. 1b), a number of

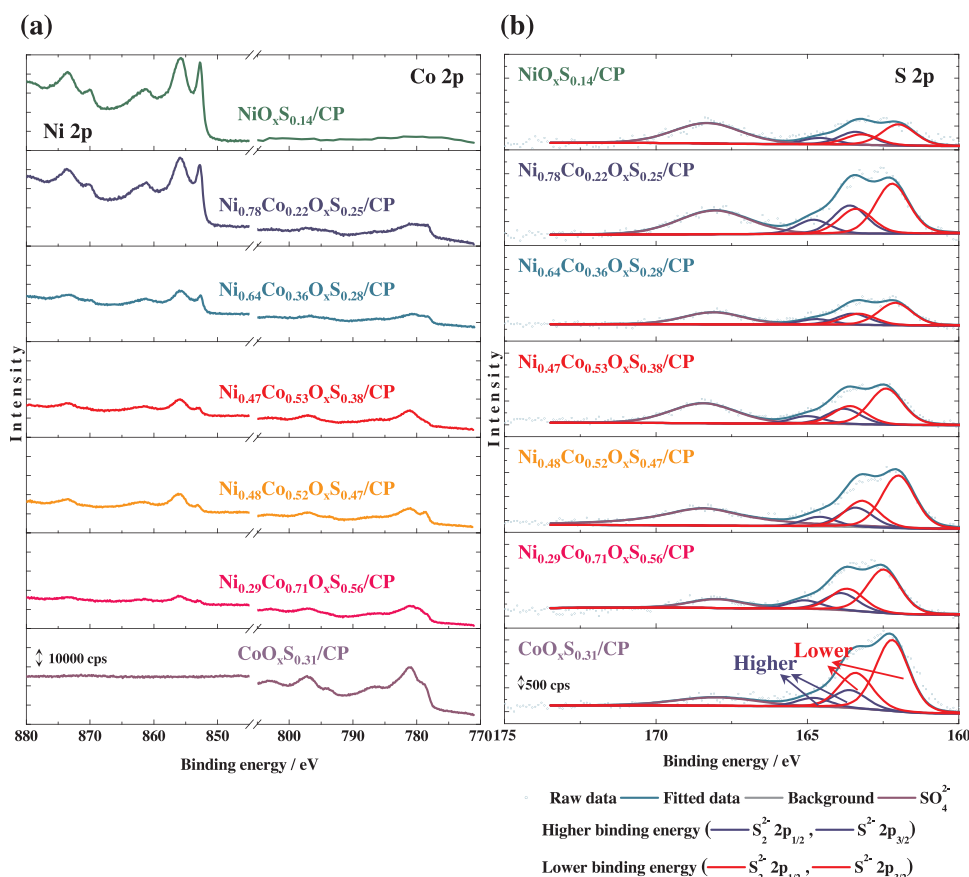


Fig. 5. XPS spectra of the  $\text{Ni}_y\text{Co}_{1-y}\text{O}_x\text{S}_z/\text{CP}$  catalysts: (a) Ni 2p and Co 2p peaks, (b) S 2p peaks. (For interpretation of the references to colour in the text, the reader is referred to the web version of this article.)

agglomerated spheres with a diameter of 4–6  $\mu\text{m}$  were observed. When 20% Co precursor was added, each sphere grew slightly in the vertical direction, forming a cylindrical shape (Fig. 1c). With a 40% ratio of the Co precursor (Fig. 1d), the branches grew in a perpendicular direction from the cylinder. Further increase in the Co precursor composition showed sharp branches with a more hierarchical structure, demonstrating the fern-like shapes as shown in Fig. 1e–h. It should be noted that the shortened branches were observed with the higher composition of Co precursor (80% and 100%). The shapes of the deposits were similar with those reported in previous literature, despite different substrates (e.g. stainless steel) used [54]. In addition, we confirmed that all deposits were uniformly formed with high coverage on the topside of the carbon fibers.

The composition of the deposits was confirmed by EDS analysis (Fig. S1), with the results summarized in Fig. 2a. As the Co precursor ratio increases in solution, the Co composition in the deposit increases linearly. Based on this composition, each deposit was named as  $\text{Ni}_y\text{Co}_{1-y}\text{O}_x/\text{CP}$  as shown in Table 1. Due to the fast formation of native oxide in air, the oxygen composition was simply expressed as  $x$  in the nomenclature. The crystal structures of  $\text{Ni}_y\text{Co}_{1-y}\text{O}_x/\text{CP}$  were examined by XRD analysis as shown in Fig. 2b. The XRD patterns were normalized by the C(002) peak at  $26.4^\circ$  (JCPDS #41-1487) from CP. We confirmed that the Ni face-centered-cubic (FCC) and Co hexagonal-close-packed (HCP) crystal structures were obtained, which agreed with a previously reported study [54]. For  $\text{NiO}_x/\text{CP}$ , the Ni(111) peak appeared at  $44.4^\circ$  (JCPDS #87-0712). With the increase in Co composition, the peak position was shifted to a lower angle, indicating the formation of NiCo alloys [55]. As the ratio of Co further increased, the peaks of the NiCo alloys became smaller and were accompanied by the Co HCP peaks appearing at  $41.5^\circ$  and  $47.5^\circ$  (JCPDS #05-0727). These patterns are well matched to previous results that show the change in crystal

structure of Ni–Co at a high Co ratio [54–56].

### 3.2. S ion exchange to fabricate fern-like $\text{Ni}_y\text{Co}_{1-y}\text{O}_x\text{S}_z/\text{CP}$

The sulfidation process was carried out on the electrodeposited transition metal oxides to fabricate the transition metal oxysulfides. For S IER, the various transition metal oxides were immersed in a 1 mM  $\text{Na}_2\text{S}$  solution at various reaction times (1, 2, 5, 10, 20, 30, and 60 min) at room temperature. Fig. S2 shows the FESEM images of  $\text{Ni}_{0.60}\text{Co}_{0.40}\text{O}_x/\text{CP}$  after S IER based on the reaction time. After 10 min, the round particles with a size of  $\sim 100$  nm appeared on the surface of  $\text{Ni}_{0.60}\text{Co}_{0.40}\text{O}_x/\text{CP}$ , which was consistent with previous literature [57,58]. However, of the overall shape of a fern-like structure was maintained. Fig. 3a demonstrates the HER overpotential at  $-10$  mA/ $\text{cm}_{\text{geo}}^2$  depending on the S IER time. To avoid the effect of S reduction [59], each potential value was obtained when the chronopotentiometry was saturated at 100 s (Fig. S3). With the increase of S IER time, the overpotential decreased gradually until 20 min and saturated thereafter. Fig. 3b shows the difference of the overpotential before and after S IER (20 min). For the  $\text{NiO}_x/\text{CP}$ ,  $\text{Ni}_y\text{Co}_{1-y}\text{O}_x/\text{CP}$  and  $\text{CoO}_x/\text{CP}$ , the overpotential decreased in the range of 0.063–0.097 V.

Fig. 4 shows the FESEM images of samples before (Fig. 4a–g) and after S IER for 20 min (Fig. 4h–n). For lower Co compositions (0–40%), the surface morphology was mostly similar. However, with higher Co compositions (49–100%), much rougher surfaces were observed along with the presence of small particles, indicating that the S IER was accelerated on the Co rather than on the Ni. Comparing lower magnification FESEM images before (Fig. 1) and after S IER for 20 min (Fig. S4), no significant changes were observed on the overall morphology. In addition, the side view EDS mapping of  $\text{Ni}_{0.60}\text{Co}_{0.40}\text{O}_x/\text{CP}$  after S IER for 20 min confirmed that the Ni, Co, and S were uniformly distributed



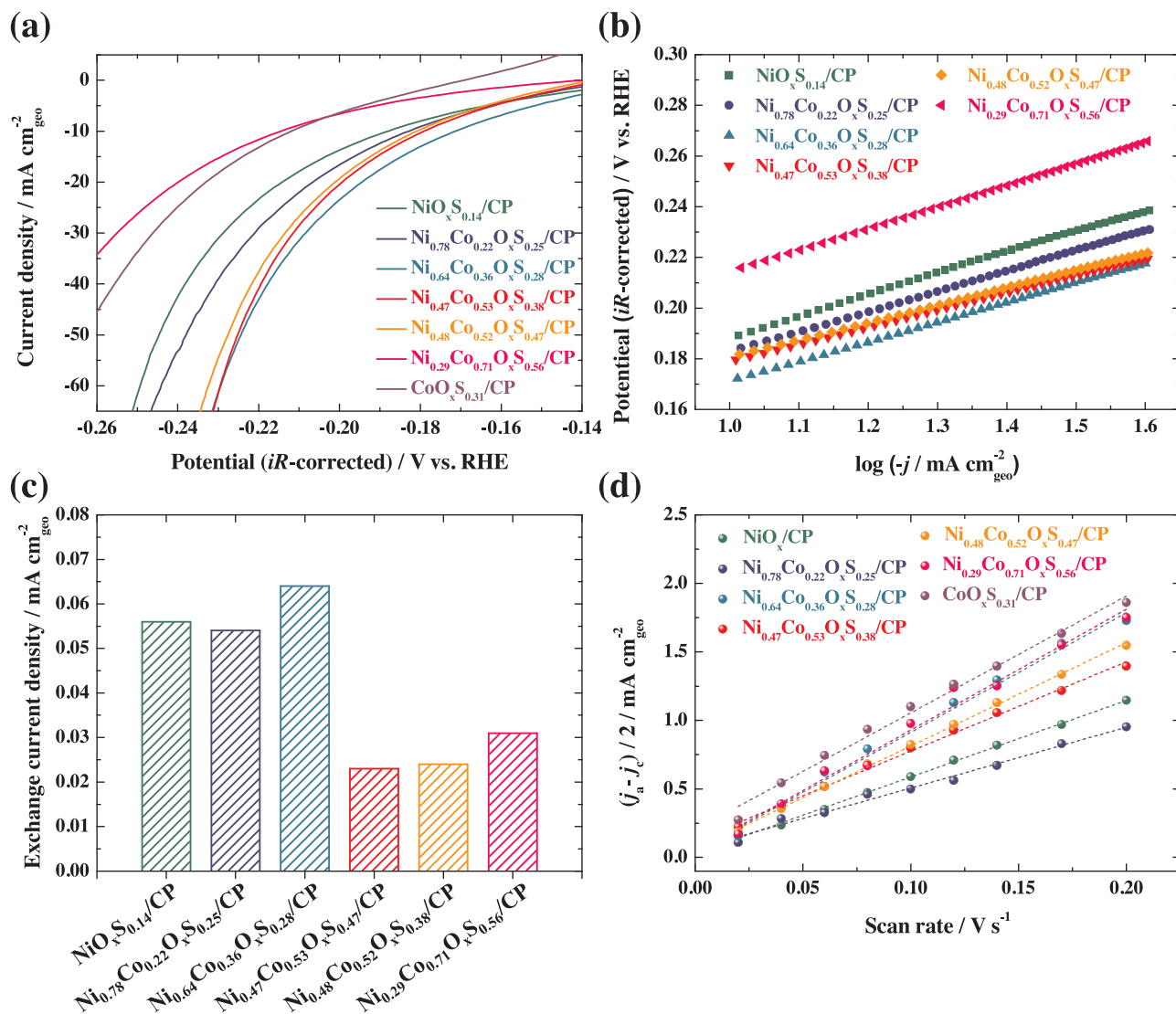


Fig. 6. (a) LSV curves for HER activity at a scan rate of 50 mV/s in a 0.5 M H<sub>2</sub>SO<sub>4</sub> electrolyte, (b) Tafel plots corresponding to (a), (c) exchange current densities for the different material systems, and (d) the measurement of double layer capacitances.

on the surface, demonstrating that the sulfidation proceeded uniformly (Fig. S5).

After S IER for 20 min, the surface composition was examined by XPS analysis as shown in Fig. 5. Based on this, each transition metal oxysulfide prepared was named as Ni<sub>y</sub>Co<sub>1-y</sub>O<sub>x</sub>S<sub>z</sub>/CP, according to their composition as summarized in Table 1. As the Co composition increases in Ni<sub>y</sub>Co<sub>1-y</sub>O<sub>x</sub>S<sub>z</sub>/CP, the S content also increased except for the CoO<sub>x</sub>S<sub>0.31</sub>/CP case, which corresponds to the morphological change (Fig. 4). This may be attributed to the difference in K<sub>sp</sub> values for Ni and Co sulfides because CoS (3 × 10<sup>-26</sup>) is lower compared to NiS (1.3 × 10<sup>-25</sup>) [36]. Fig. 5a demonstrates the Ni 2p and Co 2p spectra for Ni<sub>y</sub>Co<sub>1-y</sub>O<sub>x</sub>S<sub>z</sub>. The surface composition ratio between Ni and Co after S IER was mostly similar with the bulk composition ratio before S IER (Fig. 2a). The S 2p spectra for Ni<sub>y</sub>Co<sub>1-y</sub>O<sub>x</sub>S<sub>z</sub> were deconvoluted to the two doublets for S<sub>2</sub><sup>2-</sup> and S<sup>2-</sup> [60,61] as shown in Fig. 5b and Table S1. The intensity ratio of S 2p<sub>1/2</sub> and S 2p<sub>3/2</sub> is 1:2. The intervals between the two peaks were fixed at 1.2 eV and all full width at half maximum were constant. The peaks ratio of S atoms with higher binding energy (blue lines in Fig. 5b) was decreased by the increase in S surface composition for NiO<sub>x</sub>S<sub>0.14</sub>/CP and Ni<sub>y</sub>Co<sub>1-y</sub>O<sub>x</sub>S<sub>z</sub>/CP catalysts as summarized in Table 1.

### 3.3. HER performance of fern-like Ni<sub>y</sub>Co<sub>1-y</sub>O<sub>x</sub>S<sub>z</sub>/CP

The HER activity of the prepared catalysts was evaluated by repeated CV (100 cycles) at a scan rate of 50 mV/s in 0.5 M H<sub>2</sub>SO<sub>4</sub> solution (Fig. S6). Fig. 6a shows the forward scan of the first cycle after iR correction. The activity order for the HER obtained by CV was consistent with that of the overpotential measured at -10 mA/cm<sub>geo</sub><sup>2</sup> (Fig. 3a). It should be emphasized that the CoO<sub>x</sub>S<sub>0.31</sub>/CP was excluded in the activity comparison because it had an anodic current of catalyst dissolution in the measured potential range. At -10 mA/cm<sub>geo</sub><sup>2</sup>, the Ni<sub>0.64</sub>Co<sub>0.36</sub>O<sub>x</sub>S<sub>0.28</sub>/CP catalyst showed the lowest overpotential of -172 mV, among others. The Tafel plots demonstrate the slope (b = 2.3RT/αF) range of 67.8–85.3 mV (Fig. 6b and Table 1). After proton adsorption on all Ni<sub>y</sub>Co<sub>1-y</sub>O<sub>x</sub>S<sub>z</sub>/CP through Volmer reaction (H<sub>3</sub>O<sup>+</sup> + e<sup>-</sup> → H<sub>ad</sub> + H<sub>2</sub>O, b = 120 mV), the proton desorption is carried out following the Heyrovsky reaction (H<sub>ad</sub> + H<sub>3</sub>O<sup>+</sup> + e<sup>-</sup> → H<sub>2</sub> + H<sub>2</sub>O, b = 40 mV) rather than the Tafel reaction (H<sub>ad</sub> + H<sub>ad</sub> → H<sub>2</sub>, b = 30 mV), indicating that the electrochemical desorption is rate-determining step [62]. From the Tafel plots, the exchange current density was calculated as shown in Fig. 6c. The Ni<sub>0.64</sub>Co<sub>0.36</sub>O<sub>x</sub>S<sub>0.28</sub>/CP catalyst exhibited the highest exchange current density of 0.064 mA/cm<sub>geo</sub><sup>2</sup>, among others. To calculate the surface area of the transition metal oxysulfides, CV was conducted by varying the scan rate from 20 to

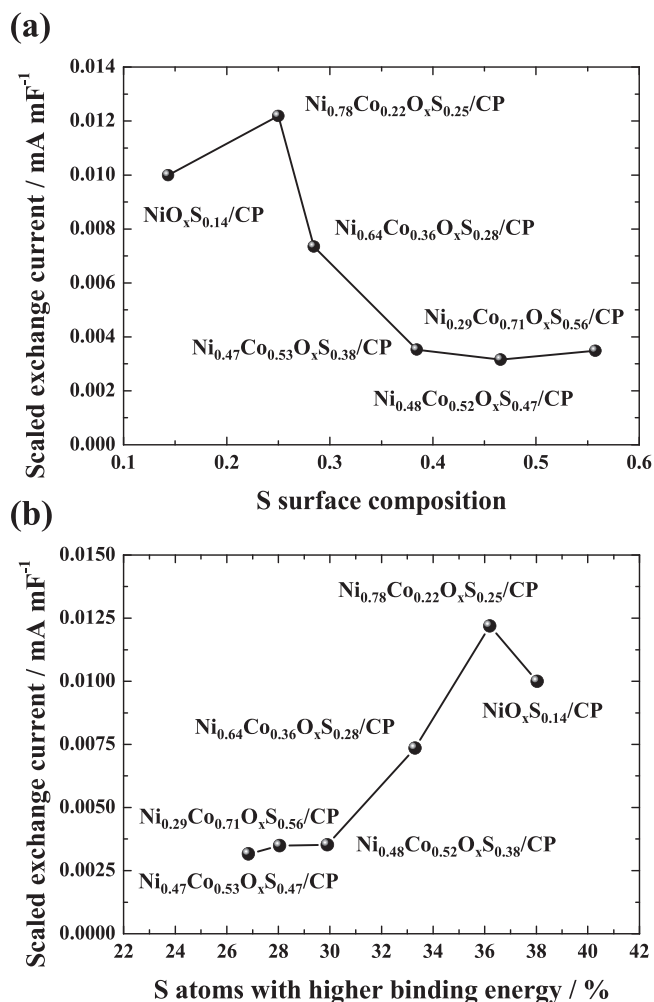


Fig. 7. Scaled exchange current according to (a) S surface composition and (b) the proportion of S atoms having higher binding energies.

200 mV/s in 1.0 M KOH solution (Fig. S7). CV was performed repeatedly until it was stabilized to avoid the effect of S reduction [63]. Fig. 6d shows the mean values of the anodic and cathodic current densities at  $-0.9 \text{ V}_{\text{SCE}}$  according to the scan rates. Subsequently, the  $C_{\text{dl}}$  was calculated using the slope after linear fitting (Table 1). At a lower Co ratio ( $\sim 0.22$ ), a smaller  $C_{\text{dl}}$  was obtained, which is consistent with their morphology confirmed by FESEM image (Fig. S4b and c). With higher Co ratios, the  $C_{\text{dl}}$  values were in the range  $6.52\text{--}8.82 \text{ mF/cm}_{\text{geo}}^2$  owing to the formation of branches (Fig. S4d–g).

To determine the intrinsic activity, the exchange current density was normalized by the  $C_{\text{dl}}$  value representing the surface roughness. Fig. 7a shows the scaled exchange current as a function of S surface composition of  $\text{Ni}_y\text{Co}_{1-y}\text{O}_x\text{S}_z/\text{CP}$ , showing a volcano relationship. For  $\text{NiO}_x\text{S}_{0.14}/\text{CP}$ , the scaled exchange current was  $0.010 \text{ mA/mF}$ . The highest value of the scaled exchange current was obtained with  $\text{Ni}_{0.78}\text{Co}_{0.22}\text{O}_x\text{S}_{0.25}/\text{CP}$  at a S surface composition of 0.25. Further increase of S surface composition showed the decrease in intrinsic activity, followed by saturation with S surface composition over 0.38. This result was similar to the case of cobalt oxysulfide, which exhibited the volcano relation as a function of S surface composition [41]. In the literature, the cobalt oxysulfide having an S ratio of 0.18 showed the maximum HER intrinsic activity owing to its suitable H adsorption energy. Fig. 7b demonstrates the significant effect of S atoms with higher binding energy on intrinsic activity. The scaled exchange current for  $\text{Ni}_y\text{Co}_{1-y}\text{O}_x\text{S}_z/\text{CP}$  catalyst was increased by the increase in S atoms of higher binding energy ratio. A similar result was reported with  $\text{MoS}_x$

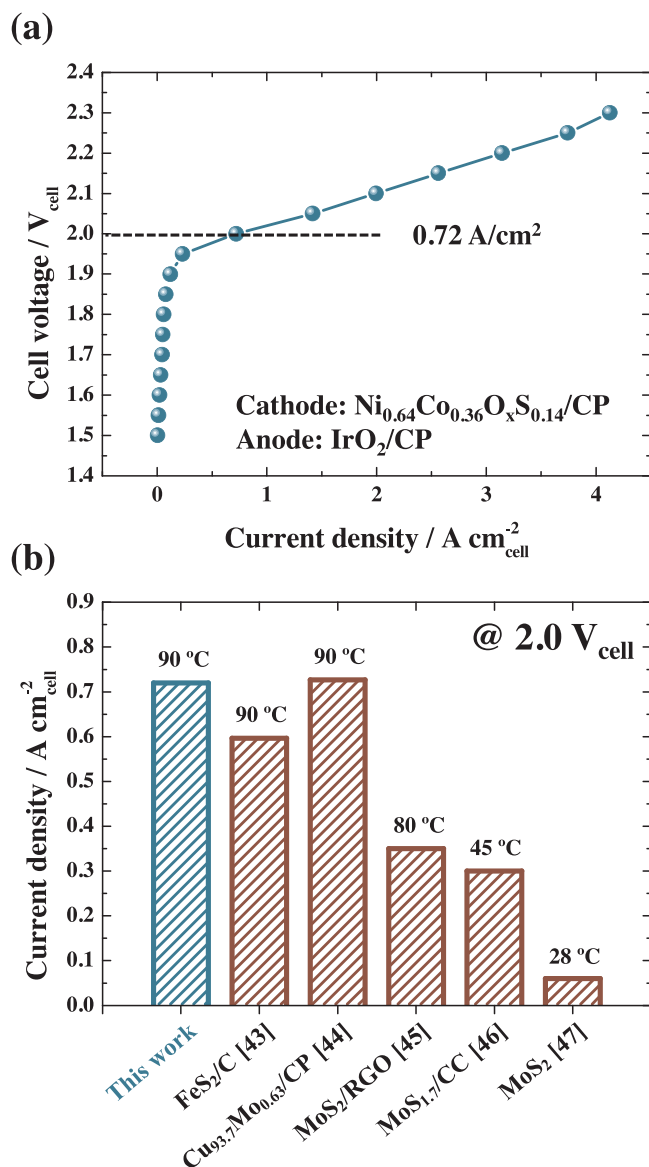


Fig. 8. (a) Polarization curve for PEMWE operation employing  $\text{Ni}_{0.64}\text{Co}_{0.36}\text{O}_x\text{S}_{0.14}/\text{CP}$  as the cathode. (b) Comparison of the PEMWE performance at  $2.0 \text{ V}_{\text{cell}}$ .

catalysts [64]. However, the  $\text{NiO}_x\text{S}_{0.14}/\text{CP}$  showed lower HER intrinsic activity even though it had the highest S atom ratio with higher binding energy (38%), implying that the bimetallic effect on the HER intrinsic activity might have occurred. Although the catalyst configuration is different, Wang et al. have reported that the addition of a small amount of Co to  $\text{FeS}_2$  modified its hydrogen adsorption energy to enhance the HER activity [65].

#### 3.4. PEMWE operation employing fern-like $\text{Ni}_y\text{Co}_{1-y}\text{O}_x\text{S}_z/\text{CP}$ cathode

Although the highest intrinsic activity was achieved with  $\text{Ni}_{0.78}\text{Co}_{0.22}\text{O}_x\text{S}_{0.25}/\text{CP}$  catalyst, in terms of practical application, the  $\text{Ni}_{0.64}\text{Co}_{0.36}\text{O}_x\text{S}_{0.28}/\text{CP}$  catalyst was chosen as a cathode to fabricate the MEA for the PEMWE operation (Fig. S8), owing to the lowest overpotential. Fig. 8a shows the polarization curves of the PEMWE employing the  $\text{Ni}_{0.64}\text{Co}_{0.36}\text{O}_x\text{S}_{0.28}/\text{CP}$  cathode and  $\text{IrO}_2/\text{CP}$  anode after the activation process. At the cell voltage of  $2.0 \text{ V}_{\text{cell}}$ , the PEMWE showed a current density of  $0.72 \text{ A/cm}^2$ . Fig. 8b shows the comparison of the current density of PEMWE at  $2.0 \text{ V}_{\text{cell}}$  reported in this work and in literatures. The PEMWE employing the  $\text{Ni}_{0.64}\text{Co}_{0.36}\text{O}_x\text{S}_{0.28}/\text{CP}$  cathode shows higher or comparable current density at the cell voltage of

2.0 V<sub>cell</sub>. The specific conditions for the PEMWE operation in this work and those reported in literature is summarized in Table S2.

#### 4. Conclusion

As cathodes for PEMWE operation, fern-like Ni<sub>3</sub>Co<sub>1-y</sub>O<sub>x</sub>S<sub>z</sub> catalysts were fabricated on a CP substrate. The simple electrodeposition technique and subsequent S IER permitted the facile fabrication of the electrode with morphological and compositional controls. With the increase in S IER time, the overpotential for the HER was significantly improved that then saturated at a S IER time of 20 min. The intrinsic activity based on the surface area showed volcano behaviors as a function of the surface composition and ratio of S having higher binding energies. The PEMWE containing the Ni<sub>0.64</sub>Co<sub>0.36</sub>O<sub>x</sub>S<sub>0.28</sub>/CP cathode demonstrated reasonably higher performance compared to the values reported in literature with non-noble cathodes, indicating its cost effectiveness for hydrogen production.

#### Acknowledgments

This research was supported by the National Research Foundation of Korea (NRF) grant funded by the Korea government MSIT (2015R1C1A1A01055708 and 2016M3A7B4909369).

#### Appendix A. Supplementary data

Supplementary material related to this article can be found, in the online version, at doi:<https://doi.org/10.1016/j.apcatb.2018.03.023>.

#### References

- [1] J.A. Turner, Science 305 (2004) 972–974.
- [2] S.E. Hosseini, M.A. Wahid, Renew. Sustain. Energy Rev. 57 (2016) 850–866.
- [3] A. Heinzel, B. Vogel, P. Hübner, J. Power Sources 105 (2002) 202–207.
- [4] B.T. Schädler, M. Duisberg, O. Deutschmann, Catal. Today 142 (2009) 42–51.
- [5] K. Zeng, D. Zhang, Prog. Energy Combust. Sci. 36 (2010) 307–326.
- [6] C. Acar, I. Dincer, Int. J. Hydrogen Energy 39 (2014) 1–12.
- [7] M. Carmo, D.L. Fritz, J. Mergel, D. Stolten, Int. J. Hydrogen Energy 38 (2013) 4901–4934.
- [8] C.G. Morales-Guio, L.-A. Stern, X. Hu, Chem. Soc. Rev. 43 (2014) 6555–6569.
- [9] Y. Zheng, Y. Jiao, L.H. Li, T. Xing, Y. Chen, M. Jaroniec, S.Z. Qiao, ACS Nano 8 (2014) 5290–5296.
- [10] T.Y. Ma, J. Ran, S. Dai, M. Jaroniec, S.Z. Qiao, Angew. Chem. Int. Ed. 54 (2015) 4646–4650.
- [11] X. Cao, Y. Han, C. Gao, Y. Xu, X. Huang, M. Willander, N. Wang, Nano Energy 9 (2014) 301–308.
- [12] D.V. Esposito, S.T. Hunt, A.L. Stottlmyer, K.D. Dobson, B.E. McCandless, R.W. Birkmire, J.G. Chen, Angew. Chem. Int. Ed. 49 (2010) 9859–9862.
- [13] D.V. Esposito, S.T. Hunt, Y.C. Kimmel, J.G. Chen, J. Am. Chem. Soc. 134 (2012) 3025–3033.
- [14] J.-S. Li, Y. Wang, C.-H. Liu, S.-L. Li, Y.-G. Wang, L.-Z. Dong, Z.-H. Dai, Y.-F. Li, Y.-Q. Lan, Nat. Commun. 7 (2016) 11204.
- [15] Y.-J. Ko, J.-M. Cho, I. Kim, D.S. Jeong, K.-S. Lee, J.-K. Park, Y.-J. Baik, H.-J. Choi, W.-S. Lee, Appl. Catal. B: Environ. 203 (2017) 684–691.
- [16] Y. Zhu, G. Chen, X. Xu, G. Yang, M. Liu, Z. Shao, ACS Catal. 7 (2017) 3540–3547.
- [17] Y. Zhang, B. Ouyang, J. Xu, S. Chen, R.S. Rawat, H.J. Fan, Adv. Energy Mater. 6 (2016) 1600221.
- [18] D.-H. Ha, B. Han, M. Risch, L. Giordano, K.P. Yao, P. Karayaylali, Y. Shao-Horn, Nano Energy 29 (2016) 37–45.
- [19] A. Laursen, K. Patraju, M. Whitaker, M. Retuerto, T. Sarkar, N. Yao, K. Ramanujachary, M. Greenblatt, G. Dismukes, Energy Environ. Sci. 8 (2015) 1027–1034.
- [20] H. Wang, Z. Lu, D. Kong, J. Sun, T.M. Hymel, Y. Cui, ACS Nano 8 (2014) 4940–4947.
- [21] J. Zeng, M. Gao, Q. Zhang, C. Yang, X. Li, W. Yang, Y. Hua, C. Xu, Y. Li, J. Mater. Chem. A 5 (2017) 15056–15064.
- [22] M. Ledendecker, H. Schlott, M. Antonietti, B. Meyer, M. Shalom, Adv. Energy Mater. 7 (2017) 1601735.
- [23] T. Tian, L. Huang, L. Ai, J. Jiang, J. Mater. Chem. A 5 (2017) 20985–20992.
- [24] S. Peng, L. Li, X. Han, W. Sun, M. Srinivasan, S.G. Mhaisalkar, F. Cheng, Q. Yan, J. Chen, S. Ramakrishna, Angew. Chem. Int. Ed. 53 (2014) 12594–12599.
- [25] C. Ranaweera, Z. Wang, E. Alqurashi, P. Kahol, P. Dvornic, B.K. Gupta, K. Ramasamy, A.D. Mohite, G. Gupta, R.K. Gupta, J. Mater. Chem. A 4 (2016) 9014–9018.
- [26] Y. Chen, S. Xu, Y. Li, R.J. Jacob, Y. Kuang, B. Liu, Y. Wang, G. Pastel, L.G. Salamanca-Riba, M.R. Zachariah, Adv. Energy Mater. 7 (2017) 1700482.
- [27] R. Miao, B. Dutta, S. Sahoo, J. He, W. Zhong, S.A. Cetegen, T. Jiang, S.P. Alpay, S.L. Suib, J. Am. Chem. Soc. 139 (2017) 13604–13607.
- [28] W. Xiao, P. Liu, J. Zhang, W. Song, Y.P. Feng, D. Gao, J. Ding, Adv. Energy Mater. 7 (2017) 1602086.
- [29] J. Hu, B. Huang, C. Zhang, Z. Wang, Y. An, D. Zhou, H. Lin, M.K. Leung, S. Yang, Energy Environ. Sci. 10 (2017) 593–603.
- [30] X. Long, G. Li, Z. Wang, H. Zhu, T. Zhang, S. Xiao, W. Guo, S. Yang, J. Am. Chem. Soc. 137 (2015) 11900–11903.
- [31] L.-L. Feng, G. Yu, Y. Wu, G.-D. Li, H. Li, Y. Sun, T. Asefa, W. Chen, X. Zou, J. Am. Chem. Soc. 137 (2015) 14023–14026.
- [32] Y. Wu, Y. Liu, G.-D. Li, X. Zou, X. Lian, D. Wang, L. Sun, T. Asefa, X. Zou, Nano Energy 35 (2017) 161–170.
- [33] H. Simchi, T.N. Walter, T.H. Choudhury, L.Y. Kirkley, J.M. Redwing, S.E. Mohnney, J. Mater. Sci. 52 (2017) 10127–10139.
- [34] L. Ma, Y. Hu, R. Chen, G. Zhu, T. Chen, H. Lv, Y. Wang, J. Liang, H. Liu, C. Yan, Nano Energy 24 (2016) 139–147.
- [35] X. Yan, X. Tong, L. Ma, Y. Tian, Y. Cai, C. Gong, M. Zhang, L. Liang, Mater. Lett. 124 (2014) 133–136.
- [36] X. Xia, C. Zhu, J. Luo, Z. Zeng, C. Guan, C.F. Ng, H. Zhang, H.J. Fan, Small 10 (2014) 766–773.
- [37] J. Li, X. Zhou, Z. Xia, Z. Zhang, J. Li, Y. Ma, Y. Qu, J. Mater. Chem. A 3 (2015) 13066–13071.
- [38] C. Ouyang, X. Wang, C. Wang, X. Zhang, J. Wu, Z. Ma, S. Dou, S. Wang, Electrochim. Acta 174 (2015) 297–301.
- [39] Y. Xue, Z. Zuo, Y. Li, H. Liu, Y. Li, Small (2017) 1700936.
- [40] W.Y. Lim, Y.F. Lim, G.W. Ho, J. Mater. Chem. A 5 (2017) 919–924.
- [41] A. Nelson, K.E. Fritz, S. Honrao, R.G. Hennig, R.D. Robinson, J. Suntivich, J. Mater. Chem. A 4 (2016) 2842–2848.
- [42] J. Liu, Y. Yang, B. Ni, H. Li, X. Wang, Small 13 (2017) 1602637.
- [43] C.D. Giovanni, Á. Reyes-Carmona, A. Coursier, S. Nowak, J.M. Grenèche, Hln. Lecoq, L. Mouton, J. Rozière, D. Jones, J. Peron, ACS Catal. 6 (2016) 2626–2631.
- [44] H. Kim, E. Hwang, H. Park, B.-S. Lee, J.H. Jang, H.-J. Kim, S.H. Ahn, S.-K. Kim, Appl. Catal. B: Environ. 206 (2017) 608–616.
- [45] T. Corrales-Sánchez, J. Ampurdanés, A. Urakawa, Int. J. Hydrogen Energy 39 (2014) 20837–20843.
- [46] A.Y. Lu, X. Yang, C.C. Tseng, S. Min, S.H. Lin, C.L. Hsu, H. Li, H. Idriss, J.L. Kuo, K.W. Huang, Small 12 (2016) 5530–5537.
- [47] S.S. Kumar, K. Selvakumar, R. Thangamuthu, A.K. Selvi, S. Ravichandran, G. Sozhan, K. Rajasekar, N. Navascues, S. Irusta, Int. J. Hydrogen Energy 41 (2016) 13331–13340.
- [48] B.-S. Lee, S.H. Ahn, H.-Y. Park, I. Choi, S.J. Yoo, H.-J. Kim, D. Henkensmeier, J.Y. Kim, S. Park, S.W. Nam, K.-Y. Lee, J.H. Jang, Appl. Catal. B: Environ. 179 (2015) 285–291.
- [49] L. Ma, S. Sui, Y. Zhai, Int. J. Hydrogen Energy 34 (2009) 678–684.
- [50] C. Rozain, E. Mayousse, N. Guillet, P. Millet, Appl. Catal. B: Environ. 182 (2016) 153–160.
- [51] V.K. Puthiyapura, M. Mamlouk, S. Pasupathi, B.G. Pollet, K. Scott, J. Power Sources 269 (2014) 451–460.
- [52] H.-S. Oh, H.N. Nong, T. Reier, M. Gliech, P. Strasser, Chem. Sci. 6 (2015) 3321–3328.
- [53] M. Cabán-Acevedo, M.L. Stone, J. Schmidt, J.G. Thomas, Q. Ding, H.-C. Chang, M.-L. Tsai, J.-H. He, S. Jin, Nat. Mater. (2015) 1245–1251.
- [54] R. Silva, S. Eugénio, T. Silva, M. Carmezim, M. Montemor, J. Phys. Chem. C 116 (2012) 22425–22431.
- [55] I. Choi, S.G. Pyo, H.-J. Kim, J.H. Jang, S.-K. Kim, Appl. Surf. Sci. 307 (2014) 146–152.
- [56] L. Wang, Y. Gao, Q. Xue, H. Liu, T. Xu, Appl. Surf. Sci. 242 (2005) 326–332.
- [57] L. Shen, J. Wang, G. Xu, H. Li, H. Dou, X. Zhang, Adv. Energy Mater. 5 (2015).
- [58] J. Chen, X. Wang, J. Wang, P.S. Lee, Adv. Energy Mater. 6 (2016) 1501745.
- [59] M.S. Faber, R. Dziedzic, M.A. Lukowski, N.S. Kaiser, Q. Ding, S. Jin, J. Am. Chem. Soc. 136 (2014) 10053–10061.
- [60] D. Wang, X. Zhang, Z. Du, Z. Mo, Y. Wu, Q. Yang, Y. Zhang, Z. Wu, Int. J. Hydrogen Energy 42 (2017) 3043–3050.
- [61] Z. Peng, D. Jia, A.M. Al-Enizi, A.A. Elzatahry, G. Zheng, Adv. Energy Mater. 5 (2015) 1402031.
- [62] D.Y. Chung, J.W. Han, D.-H. Lim, J.-H. Jo, S.J. Yoo, H. Lee, Y.-E. Sung, Nanoscale 7 (2015) 5157–5163.
- [63] B. You, Y. Sun, Adv. Energy Mater. 6 (2016) 1502333.
- [64] L.R.L. Ting, Y. Deng, L. Ma, Y.-J. Zhang, A.A. Peterson, B.S. Yeo, ACS Catal. 6 (2016) 861–867.
- [65] D.-Y. Wang, M. Gong, H.-L. Chou, C.-J. Pan, H.-A. Chen, Y. Wu, M.-C. Lin, M. Guan, J. Yang, C.-W. Chen, J. Am. Chem. Soc. 137 (2015) 1587–1592.